Supplementary Information for

Observation of intrinsic transverse thermoelectricity in anisotropic semimetals

Xinrong Zuo[1,2,3,4], Wenxuan Chen[1,2,3,4], Xuhui Mao[1,2,3,4], Xunbing Cai[1,2,3,4] & Zhenghua An[1,2,3,4*]

1 State Key Laboratory of Surface Physics, Department of Physics, Fudan University, Shanghai 200438, China.

2 Institute for Nanoelectronic Devices and Quantum Computing, Fudan University, Shanghai 200438, China.

3 Shanghai Key Laboratory of Metasurfaces for Light Manipulation, Shanghai 200438, China.

4 Shanghai Branch, Hefei National Laboratory, Shanghai 201315, China.

*Corresponding authors: anzhenghua@fudan.edu.cn.

Table of contents

Note 1 | Isotropic thermoelectric (TE) transport model.

In the isotropic TE transport model, the intrinsic physical properties of the material—specifically the electrical conductivity (σ), thermal conductivity (κ), and the Seebeck coefficient (S)—are assumed to be independent of the crystallographic direction. Consequently, these parameters are treated as scalar quantities (or uniform diagonal matrices) rather than full rank-3 tensors. This assumption simplifies the theoretical framework while establishing a baseline for understanding the fundamental coupling between electrical and thermal fields.

The basic theoretical framework for steady-state TE transport is governed by the coupled conservation equations of charge and thermal energy, alongside their respective constitutive relations. The local charge transport is described by the generalized Ohm's law, which incorporates the thermally driven current (Seebeck effect):

$$\boldsymbol{J} = -\sigma \cdot (\nabla V + S \cdot \nabla T) \tag{S1}$$

where $\boldsymbol{J}$ is the electrical current density vector, V is the electrical potential, and T is the absolute temperature. Under steady-state conditions, charge conservation dictates that the divergence of the current density is zero:

$$\nabla \cdot \boldsymbol{J} = 0 \tag{S2}$$

Simultaneously, the heat transport is described by the generalized Fourier's law, which includes the heat carried by the charge carriers (Peltier effect):

$$q = -\kappa \nabla T + STJ \tag{S3}$$

where q is the total heat flux vector. The term STJ corresponds to the Peltier heat flux (with $\Pi = ST$ according to the Kelvin relation). The steady-state energy conservation equation is given by:

$$-\nabla \cdot q + Q = 0 \tag{S4}$$

where Q represents the internal volumetric heat generation. In the presence of electrical current, the primary heat source is Joule heating, defined as $QJ = J \cdot E = |J|^2/\sigma$. Furthermore, the divergence of the Peltier heat flux inherently accounts for both the localized Peltier heating/cooling at interfaces (or spatial gradients of S) and the Thomson effect resulting from temperature gradients.

Note 2 | Anisotropic TE transport model in Td-WTe_2.

Building upon the basic scalar TE framework, the formulation must be extended to account for the strong crystalline anisotropy inherent to Td-WTe_2. As an orthorhombic semimetal(*1*) (space group $Pmn2_1$(*2*)), its transport properties exhibit significant directional dependence, fundamentally altering the interplay between charge and heat flows.

Crystallographic correspondence of transport tensors

In the anisotropic regime, the intrinsic physical properties—the electrical conductivity (σ), thermal conductivity (κ), and the Seebeck coefficient (S)—are no longer scalars but must be treated as third-rank tensors. We define the principal crystallographic coordinate system such that the x, y, and z axes align with the a-axis (the W-W zigzag-chain direction), b-axis, and c-axis (the out-of-plane van der Waals stacking direction) of the Td-WTe_2 crystal, respectively, with θ denoting the angle between the externally applied driving current and the a-axis.

When the driving electrical field is perfectly aligned with these principal axes, the transport tensors are strictly diagonal. Taking the Seebeck coefficient tensor S_0 as an example, it is expressed as:

$$S_0 = \begin{pmatrix} S_a & 0 & 0 \\ 0 & S_b & 0 \\ 0 & 0 & S_c \end{pmatrix} \tag{S5}$$

Similarly, σ_0 and κ_0 take the same diagonal form, with elements $(\sigma_a,\ \sigma_b,\ \sigma_c)$ and $(\kappa_a,\ \kappa_b,\ \kappa_c)$ characterizing the transport capabilities along the respective crystallographic axes. Under this principal alignment, current and heat flux flow parallel to the applied electric field and temperature gradient, respectively, without inducing transverse responses.

Tensor evolution under non-axial driving currents

In practically fabricated devices, especially those featuring complex geometries like asymmetric nanoconstrictions, the current path often deviates from the principal crystallographic axes. Experimentally, Td-WTe_2 flakes were obtained by mechanical exfoliation. The long edges typically align with the crystallographic *a*-axis (corresponding to the W-W zigzag-chain direction)(*3*), a morphology commonly attributed to the lower cleavage energy and preferred in-plane fracture along this direction(*4*). The precise orientation of the crystallographic axes for each selected flake was further confirmed by polarized Raman spectroscopy(*5*) (see more details in Fig.S1).

To model transport under such off-axis driving, the intrinsic diagonal tensors must be transformed into the device coordinate system. Consider a device fabricated on the cleavage plane (*ab*-plane) of WTe_2, where the primary current channel (device *x*-axis) forms an angle θ relative to the crystallographic *a*-axis. This spatial evolution is governed by a standard rotation matrix $R(\theta)$ around the *c*-axis:

$$R(\theta) = \begin{pmatrix} \cos(\theta) & -\sin(\theta) & 0 \\ \sin(\theta) & \cos(\theta) & 0 \\ 0 & 0 & 1 \end{pmatrix} \tag{S6}$$

The effective transport tensors in the device coordinate system are obtained via the transformation $T(\theta) = R(\theta) \cdot T(\theta = 0) \cdot R^T(\theta)$, where T represents σ, κ, or S. Consequently, the transformed Seebeck tensor $S(\theta)$ evolves into:

$$T(\theta)= \begin{pmatrix} \frac{S_a+S_b}{2} + \frac{S_a-S_b}{2}\cos(2\theta) & \frac{S_a-S_b}{2}\sin(2\theta) & 0 \\ \frac{S_a-S_b}{2}\sin(2\theta) & \frac{S_a+S_b}{2} - \frac{S_a-S_b}{2}\cos(2\theta) & 0 \\ 0 & 0 & S_c \end{pmatrix} \tag{S7}$$

Crucially, for any non-axial driving condition where the current deviates from the principal crystallographic axes, the off-diagonal components (e.g., $S_{xy} = S_{yx} = \frac{S_a-S_b}{2}\sin(2\theta)$) become non-zero. These non-zero off-diagonal terms mathematically dictate the generation of transverse thermoelectric effects (such as the transverse Peltier effect), wherein an applied longitudinal electrical current inherently drives a transverse heat flux. Furthermore, owing to the periodic nature of the $\cos(2\theta)$ and $\sin(2\theta)$ functions, the transport tensors possess a 180° rotational invariance, with the transverse TE response reaching its maximum magnitude at $\theta =$ 45° and 135°.

Numerical simulation implementation

The anisotropic generalized Ohm's law and Fourier's law were implemented in COMSOL Multiphysics 6.2, integrating the full 3×3 matrices derived above. The governing coupled equations are adapted as:

$$\boldsymbol{J} = -\hat{\sigma}(\theta) \cdot \left(\nabla V + \hat{S}(\theta) \cdot \nabla T\right) \tag{S8}$$

$$q = -\hat{\kappa}(\theta)\nabla T + \hat{S}(\theta)T\boldsymbol{J} \tag{S9}$$

In the experimental results for Td-WTe_2, the TE signal exhibits a linear dependence on the applied bias, suggesting a Peltier-dominated mechanism(*6*) associated with the spatial anisotropy of the Seebeck coefficient, $S(\boldsymbol{r})$. Notably, the measured lattice temperature rise due to Joule heating is remarkably small (approximately 0.4 K). This minimal temperature excursion effectively rules out the contribution of the Thomson effect(*7, 8*), which would otherwise arise from the temperature-dependent Seebeck coefficient $S(T)$. Furthermore, considering the charge continuity equation ($\nabla \cdot \boldsymbol{J} = 0$ as shown in Eq. S2), the TE heat generation in our system is solely governed by the Peltier term, namely:

$$\dot{q} = (\nabla_r S) T \boldsymbol{J} \tag{S10}$$

In the COMSOL environment, the *Electric Currents* and *Heat Transfer in Solids* modules were defined with these user-specified tensor materials rather than isotropic materials. During the simulation, a fixed ambient temperature boundary condition ($T_0 = 300\ K$) was applied at the substrate base, while an external sweeping bias was applied at the electrical terminals. The finite element solver simultaneously calculated the localized Joule heating ($\boldsymbol{J} \cdot E$) and the anisotropic Peltier heat generation/absorption $(\nabla_r S) T \boldsymbol{J}$. Due to the tensor nature of the transport parameters, the simulation captures how the transverse TE heat flux constructively accumulates at the constriction edges. This allows us to theoretically map the parameter space and accurately reproduce the bias evolution where local absolute cooling outpaces Joule heating.

Supplementary References

1. Z. Fei *et al.*, Ferroelectric switching of a two-dimensional metal. *Nature* **560**, 336-339 (2018).
2. J. Xiao *et al.*, Berry curvature memory through electrically driven stacking transitions. *Nat. Phys.* **16**, 1028-1034 (2020).
3. Y.-X. Wang *et al.*, Visualization of bulk and edge photocurrent flow in anisotropic Weyl semimetals. *Nat. Phys.* **19**, 507-514 (2023).
4. Y. Wang *et al.*, Gate-tunable negative longitudinal magnetoresistance in the predicted type-II Weyl semimetal WTe_2. *Nat. Commun.* **7**, 13142 (2016).
5. J. Deng *et al.*, Tuning the Decay Length of Long-Range Photocurrent in Weyl Semimetals by Engineering the Weighting Field. *Nano Lett.* **25**, 17511-17519 (2025).
6. T. Völkl *et al.*, Demonstration and imaging of cryogenic magneto-thermoelectric cooling in a van der Waals semimetal. *Nat. Phys.* **20**, 976-983 (2024).
7. A. Takahagi *et al.*, Observation of the transverse Thomson effect. *Nat. Phys.* **21**, 1283-1289 (2025).
8. Z. Chen, X. Zhang, S. Zhang, J. Luo, Y. Pei, Demonstration of efficient Thomson cooler by electronic phase transition. *Nat. Mater.* **24**, 34-38 (2025).

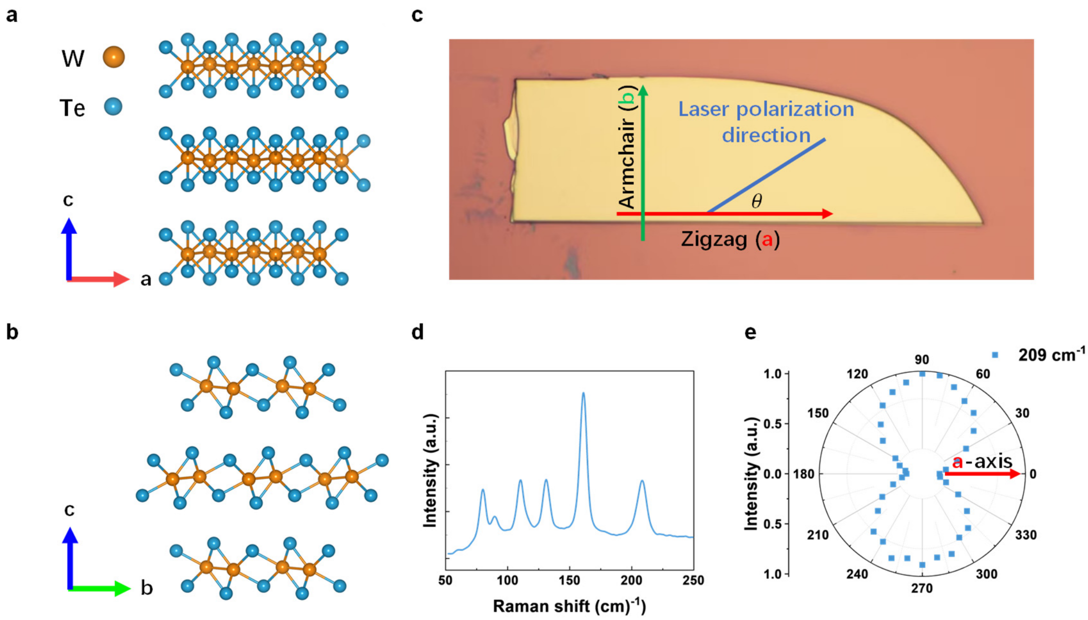

Fig. S1 | Crystal structure and anisotropic Raman spectrum of Td-WTe_2. **a**,**b**, Schematic crystal structures viewed along the *a* axis (**a**, W-W chains) and the b axis (**b**, Te-W chains), respectively. **c**, Mechanically exfoliated WTe_2 flake, whose long edge is identified as the zigzag (*a* axis); the angle between the laser polarization and the *a* axis is denoted as θ. **d**, Raman spectrum measured with the laser polarization aligned along the *a* axis. **e**, Anisotropic Raman spectra acquired for different laser polarization directions.

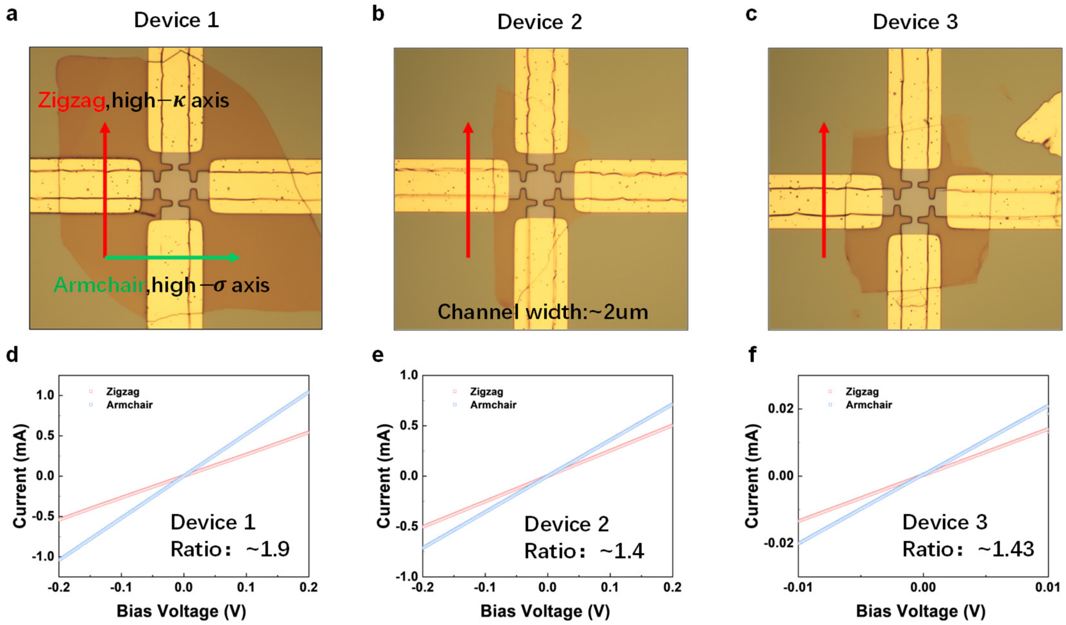

Fig. S2 | Four-terminal nanoconstriction devices and anisotropic conductivity. **a-c**, Optical micrographs of four-terminal nanoconstriction devices with current flowing along principal crystallographic axes; the channel width is approximately 2 μm. **d-f**, I-V characteristics of the corresponding devices, all exhibiting anisotropic electrical conduction, with higher conductivity along the armchair direction. The conductivity ratio σ_b/σ_a ranges from 1.4 to 1.9.

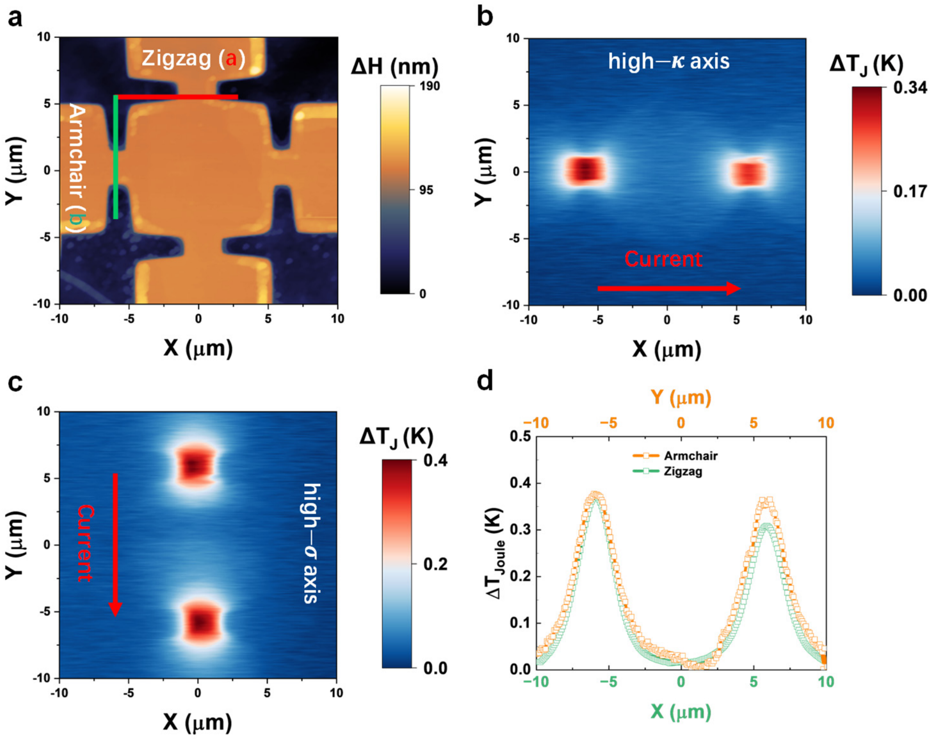

Fig. S3 | Weakly anisotropic 2D distribution of Joule heating. a, AFM image of four-terminal nanoconstriction devices with current flowing along principal crystallographic axes; the device thickness is approximately 190 nm. **b**,**c**, 2D spatial distributions of Joule heating for current flowing along the *a* axis and the *b* axis, respectively. **d**, 1D line scans of the Joule heating extracted from **b** and **c**.

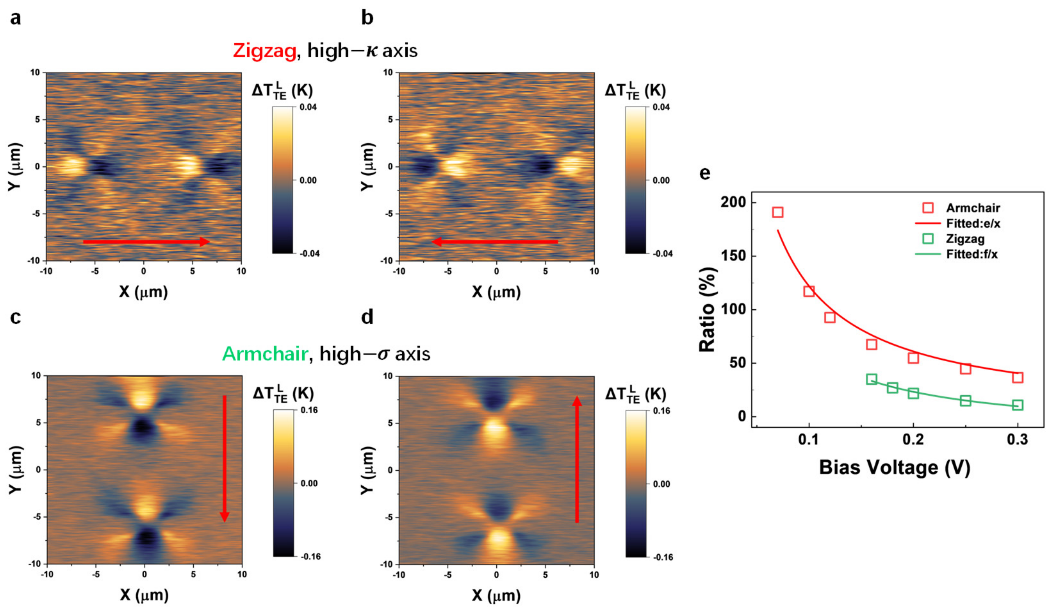

Fig. S4 | Anisotropic 2D distribution of TE response and axis-aligned TE efficiency. a,**b**, 2D TE maps for current along the *a* axis under positive (**a**) and negative (**b**) bias. **c**,**d**, Corresponding TE maps for current along the *b* axis under positive (**c**) and negative (**d**) bias. **e**, Bias-dependent anisotropic TE efficiency, quantified by the ratio: $\frac{\Delta T_{\mathrm{J}}}{\Delta T_{\mathrm{TE}}} \times 100$ %. All 2D TE measurements are performed at a bias voltage of AC 0.3 V.

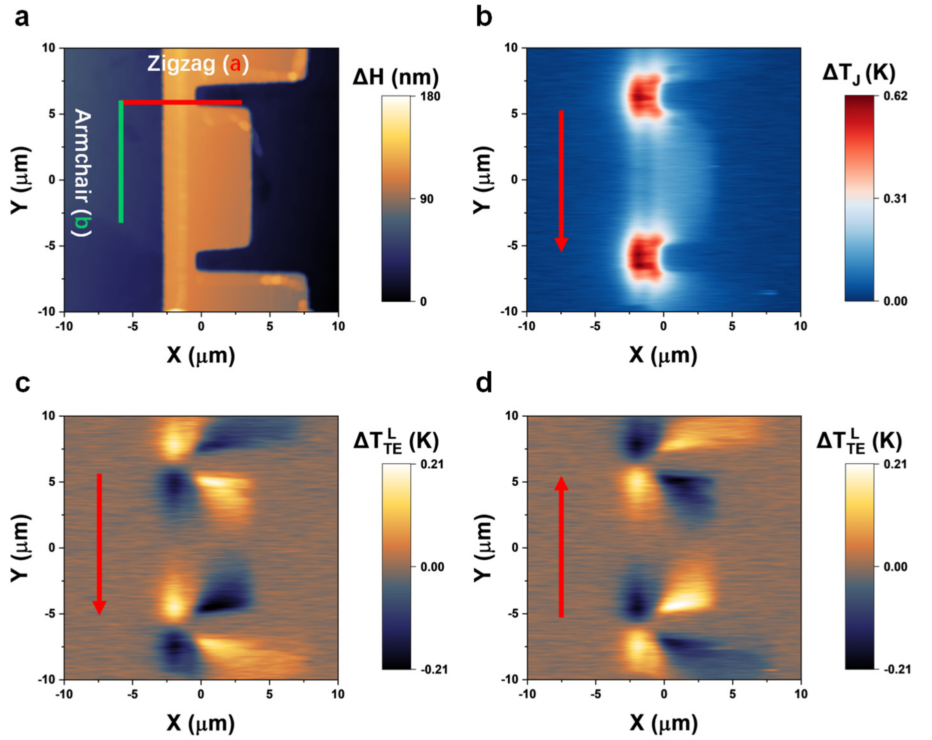

Fig. S5 | Anisotropic 2D distributions of Joule heating and TE response in the asymmetric device. **a**, AFM image of the asymmetric device with current flowing along the *b* axis; the flake thickness is ~180 nm. **b**, Spatial map of the corresponding Joule heating. **c**,**d**, 2D TE response obtained under positive (**c**) and negative (**d**) bias, illustrating the bias-polarity-dependent TE behavior.

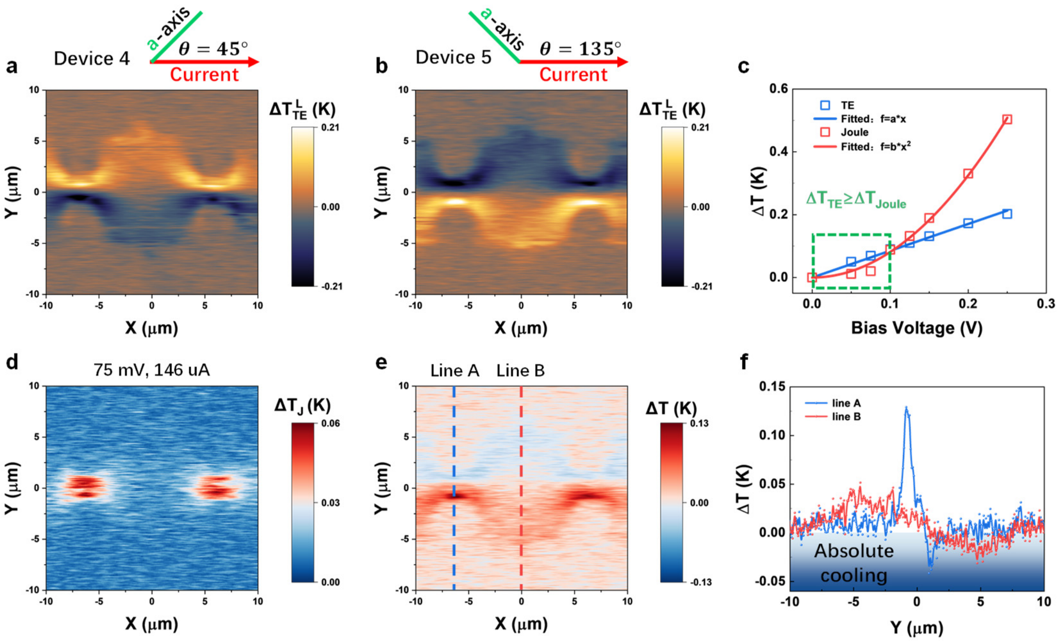

Fig. S6 | Transverse TE effect and absolute cooling. **a**, 2D map of the TE temperature change for current flowing at 45° with respect to the *a* axis. **b**, Corresponding TE map for current oriented at 135° relative to the *a* axis. **c**, Bias dependence of Joule heating and the TE response; within the green dashed region, $\Delta T_{\mathrm{TE}} \geq \Delta T_{\mathrm{J}}$, indicating the onset of absolute cooling. **d**, Spatial distributions of Joule heating and the TE signal at a bias of 75 mV. **e**, Current-induced local excess temperature ($\Delta T = \Delta T_{\mathrm{J}} + \Delta T_{\mathrm{TE}}$) with respect to the base temperature $T_0 = 300\,K$. **f**, Line profiles of the excess temperature ΔT along the line A and B, blue segments mark regions where the local temperature drops below T_0, that is, absolute cooling.

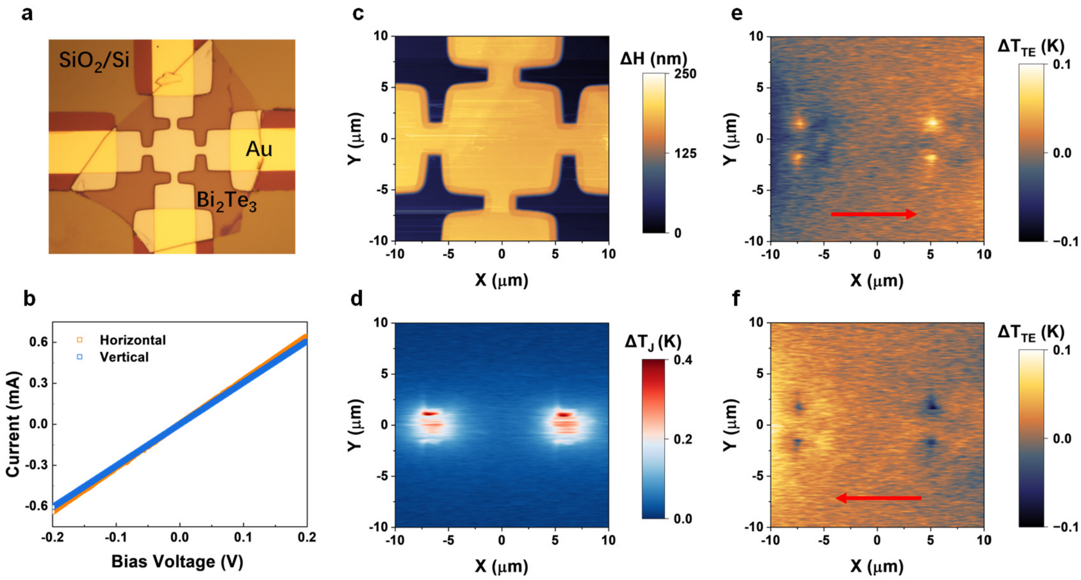

Fig. S7 | Isotropic TE response in Bi_2Te_3 device. **a**, Optical micrograph of the four-terminal Bi_2Te_3 device**. b**, I-V characteristics measured for horizontal and vertical current flow, showing clearly isotropic transport. **c**, AFM image of the device, with a flake thickness of ~250 nm. **d**, Corresponding 2D spatial map of Joule heating. **e**,**f**, TE signal distributions under positive (**e**) and negative (**f**) bias. The overall sloping TE background arises from the Au-Bi_2Te_3 ohmic junction.

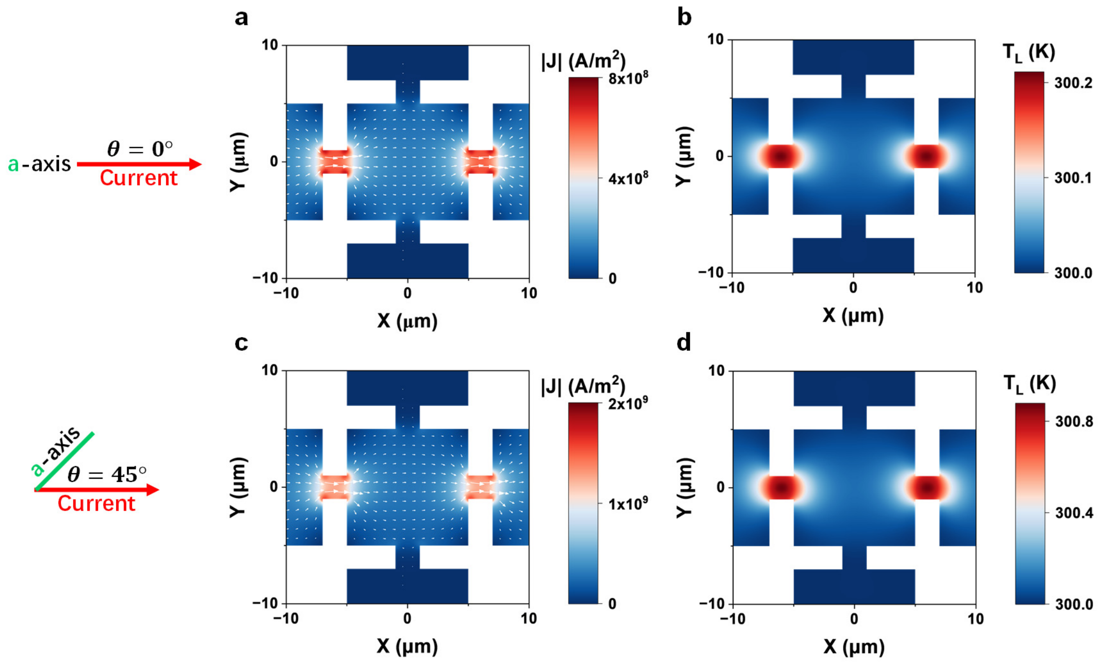

Fig. S8 | Simulated crystal-axis-dependent current density and lattice temperature. **a**,**b**, Calculated spatial distributions of current density (**a**) and lattice temperature (**b**) for current flowing along the *a* axis. **c**,**d**, Similar simulations for current oriented at 45° with respect to the *a* axis. While the overall spatial patterns of current density and lattice temperature remain resemble for different crystal orientations, their magnitudes differ markedly due to the anisotropic electrical conductivity.

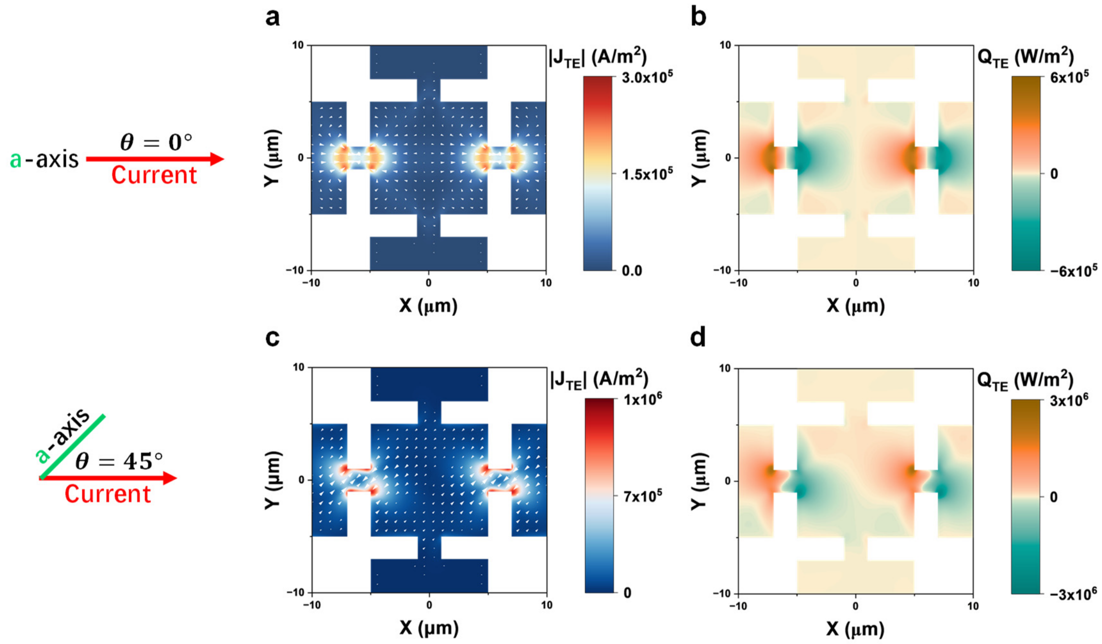

Fig. S9 | Crystal-axis dependence of simulated TE current, energy density, and non-collinearity. **a**,**b**, Calculated spatial distributions of the TE current density (**a**) and TE power density (**b**) for current flowing along the *a* axis, where the simulated power density closely reproduces the experimentally observed TE temperature profile. **c**,**d**, Corresponding simulations for current oriented at 45° with respect to the *a* axis. In this case, the TE current density is predominantly orthogonal to the drive current, revealing a transverse thermoelectric response. In Fig. **d**, the calculated TE power density is rotated relative to the experimentally applied bias and the observed TE temperature distribution, revealing a non-collinear TE energy flow in anisotropic materials that deviates from the final temperature profile, consistent with an effective rotation of the Seebeck tensor.

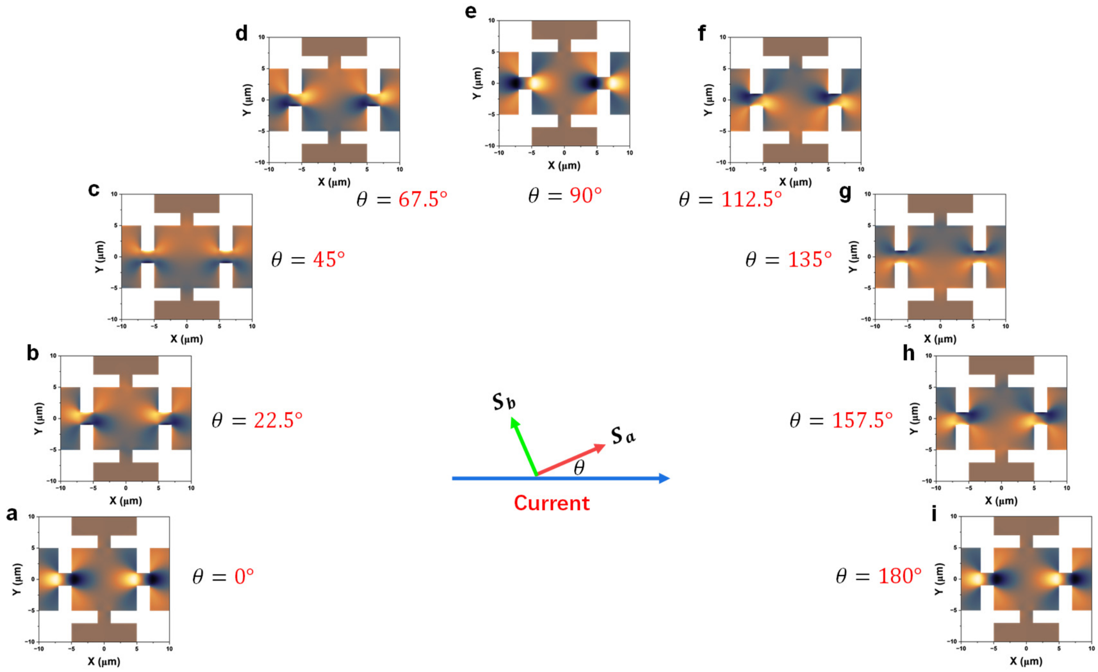

Fig. S10 | Orientation-dependent evolution of the simulated 2D TE response. In these simulations, the driving current flows horizontally from left to right, and the angle between the crystallographic *a* axis and the current direction is denoted as θ. It can be observed that, as described by Eq. S7, the rotation exhibits a periodicity of 180°, and the transverse component reaches its maximum at 45° and 135°.

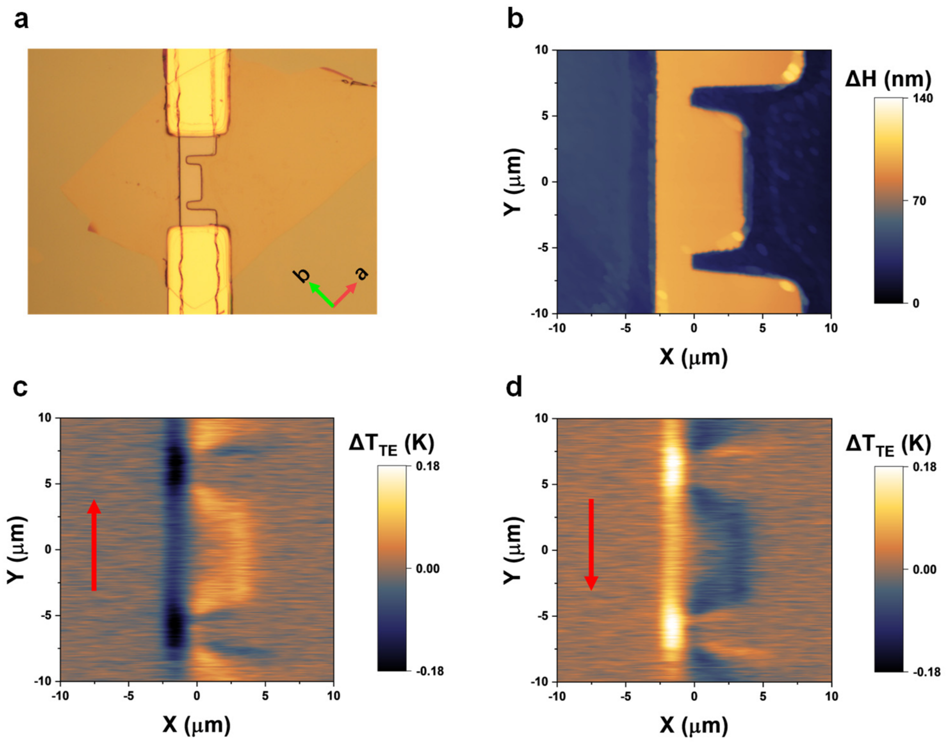

Fig. S11 | Transverse TE response in the asymmetric device. **a**,**b**, Optical and AFM images of the asymmetric device, with the crystallographic axes indicated by the coordinate frame in Fig. **a**; the flake thickness is ~140 nm. **c**,**d**, 2D TE maps recorded under positive (**c**) and negative (**d**) bias, revealing a bias-polarity-dependent transverse TE response. As discussed in the main text, by reversing the driving direction of the current, the spatial locations of cooling and heating can be freely switched, exhibiting a current-driven reversible behavior.

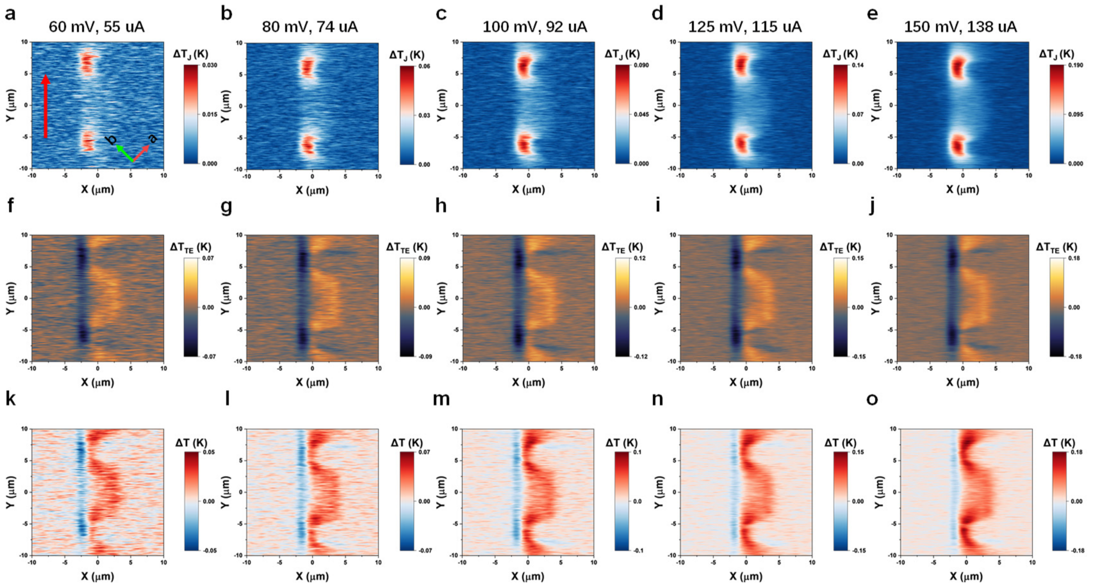

Fig. S12 | Evolution of absolute cooling with bias voltage. **a-e**, Spatial maps of Joule heating: ΔT_{J}. **f-j**, Corresponding TE temperature distributions: ΔT_{TE}. **k-o**, local excess temperature ($\Delta T = \Delta T_{\mathrm{J}} + \Delta T_{\mathrm{TE}}$) with respect to the base temperature $T_0 = 300\ K$.

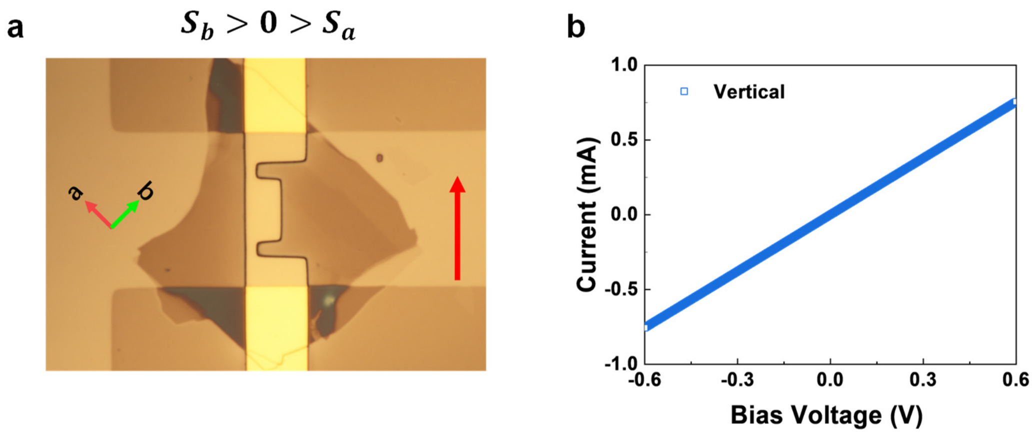

Fig. S13 | Asymmetric-channel device based on $TaIrTe_4$. a, Optical micrograph of a $TaIrTe_4$ asymmetric-channel device. The long straight natural edge formed after exfoliation defines the *a* axis, while the *b* axis is perpendicular to it. Notably, the Seebeck coefficients along the *a* and *b* axes have opposite signs. **b,** Current–voltage (I–V) characteristics of the $TaIrTe_4$ asymmetric-channel device.

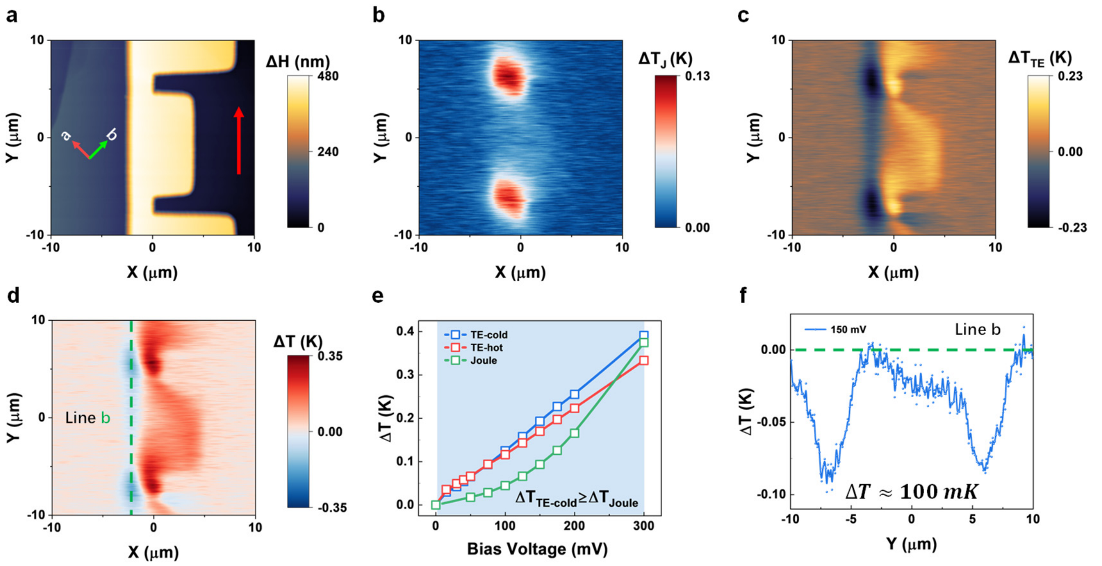

Fig. S14 | Absolute cooling in a TaIrTe$_4$ asymmetric-channel device at 300 K. **a**, AFM images of the asymmetric device, with the crystallographic axes indicated by the coordinate frame in Fig. **a**; the flake thickness is ~480 nm. **b**,**c**, 2D Joule (**b**) and TE maps (**c**) at bias voltage of 150 mV. **d**, Corresponding map of the local excess temperature ($\Delta T = \Delta T_{\mathrm{J}} + \Delta T_{\mathrm{TE}}$) with respect to the base temperature $T_0 = 300\ K$. **e**, Bias dependence of Joule heating and the TE response. In the blue-shaded region, $\Delta T_{\mathrm{TE-cold}} \geq \Delta T_{\mathrm{J}}$, indicating the onset of absolute cooling. **f**, Line profiles of the excess temperature ΔT along the line b, showing that the local temperature drops to about $100\ mK$ below T_0.